IOP Publishing Phys. Scr. 98 (2023) 025213 https://doi.org/10.1088/1402-4896/acb23b

Physica Scripta

OPEN ACCESS

RECEIVED
27 August 2022

REVISED
7 December 2022

ACCEPTED FOR PUBLICATION
11 January 2023

PUBLISHED
24 January 2023

PAPER

Multiscale modeling of complex fluids under SAOS and LAOS using a combined FENE transient network model

R O Vargas[1], **A Gómez-López**[2], **J P Escandón**[1], **R Mil-Martínez**[3] **and T N Phillips**[4,*]

[1] Instituto Politécnico Nacional, SEPI-ESIME Azcapotzalco, Av. de las Granjas 682, Col. Santa Catarina, Alcaldía Azcapotzalco, Ciudad de México, 02250, Mexico
[2] Universidad Nacional Autónoma de México, FES Cuautitlán, Departamento de Ingeniería, Sección Mecánica, Av. Teoloyucan Km 2.5, Col. San Sebastián Xhala, Cuautitlán Izcalli, Estado de México, 54714, Mexico
[3] Escuela Militar de Ingenieros, Universidad del Ejército y Fuerza Aérea, Escuela Militar de Ingenieros, Av. Industria Militar No.261, Col. Lomas de San Isidro, Naucalpan de Juárez, Edo. Mex. 53960, Mexico
[4] School of Mathematics Cardiff University, Senghennydd Road Cardiff CF24 4AG United Kingdom
[*] Author to whom any correspondence should be addressed.

E-mail: PhillipsTN@cardiff.ac.uk

Keywords: LAOS, multiscale, viscoelasticity, transient network model

Abstract

The multiscale modeling of complex fluids under small and large amplitude oscillatory shear flow using non-linear kinetic and transient network models is presented. The kinetics of microstates is analogous to chemical kinetics, which defines the physical macromolecule interaction in a Newtonian fluid, and the concentration of microstates defines a variable maximum length of extension for each microstate. The effect of important parameters like viscosity ratio, chain length, viscoelasticity, kinetic rate constants, for different initial entanglement scenarios (entangled, disentangled and aleatory) are analyzed. The Lissajous curves for the shear stress and the first normal stress difference versus the instantaneous strain or strain-rate are shown. The self-intersection of the Lissajous curves or secondary loops is shown to depend on the kinetic rate constants, the maximum extension length, and the elasticity.

Nomenclature

Latin letters	
A	Dimensionless forward kinetic rate constant
B	Dimensionless backward kinetic rate constant
b	Dimensionless maximum extension length
d	Dimensions of the problem
C_i	Concentration of the microstate i
LC	Lissajous curve
De	Deborah number
$\mathbf{F}$	Spring force
Gn	Dimensionless complex number for oscillatory behaviour
k	Boltzmann constant
k_i^A	forward kinetic rate constants
k_i^B	backward kinetic rate constant
l_i	characteristic maximum extension length for the microstate i
$\mathbf{Q}$	Dumbbell configuration vector
Q_0	Maximum strain distance of the dumbbell
Re	Reynolds number
t	Time
T	Temperature
$\mathbf{v}$	Velocity vector

(Continued.)

Latin letters	
Wi	Weissenberg number
$\mathbf{x}$	Position vector

Greek letters	
α_i	Model parameter
β	Viscosity ratio coefficient
γ	Shear tensor
γ_0	Characteristic shear
γ_{xy}	Shear strain
$\dot{\gamma}$	Strain rate tensor
$\dot{\gamma}_0$	Characteristic strain rate
$\dot{\gamma}_{xy}$	Shear strain rate
ς	Drag coefficient
η	Viscosity function
η_0	Viscosity at zero strain rate
η_s	Solvent viscosity
η_p	Polymer viscosity
λ	Relaxation time
ν_i	Viscous coefficient for the microstate i
$\boldsymbol{\kappa}$	Transposed strain rate tensor
ρ	Density
$\boldsymbol{\sigma}$	Total stress tensor
σ_{xy}	Shear stress
$\boldsymbol{\sigma}^s$	Solvent stress tensor
$\boldsymbol{\sigma}^p$	Polymeric stress tensor
τ_i	Relaxation coefficient for the microstate i
$\boldsymbol{\Phi}$	Wiener process
$\hat{\phi}$	Angle of oscillatory behaviour
ω	Oscillation frequency
ω_i	Microstate i

1. Introduction

In rheology, oscillatory shear flow is used to investigate different materials like complex fluids and soft matter, including polymer solutions and melts, biological macromolecules, surfactants, polyelectrolytes, suspensions and emulsions [1]. This dynamical test is divided into two regimes, linear (small amplitude oscillatory shear, SAOS) and nonlinear (large amplitude oscillatory shear, LAOS). At SAOS, the rheological properties do not depend on the strain amplitude, and the sinusoidal stress or strain amplitude input results in a sinusoidal response. On the other hand, at LAOS the rheological properties depend systematically on the strain amplitude, so that a sinusoidal strain input often results in a deviation in the shape of the resulting stress waveform from a sinusoidal wave. Hyun *et al* proposed an intermediate region between SAOS and LAOS called MAOS (medium amplitude oscillatory shear) [2]. The nonlinear response at large strain amplitude means that the familiar material functions used to quantify linear behavior in SAOS tests (the storage and loss modulus) are no longer sufficient, due to the presence of higher harmonic contributions. To describe the nonlinear response, different methods have been proposed, such as the Fourier transform [3], Stress Decomposition (SD) [4], sets of simplified characteristic functions and orthogonal polynomials [5, 6], analyzing the sequence of physical processes (SPP) [7, 8].

The purpose of dynamic oscillatory tests is to investigate nonlinear viscoelastic material responses, in order to relate nonlinear behavior with microstructure or topology, and to provide useful information for materials processing operations under large strains [1]. Wyss *et al* introduced a technique called strain-rate frequency superposition (SRFS) for probing the nonlinear structural relaxation of metastable soft materials [9]. The evolution in the shape of the distorted stress waveforms can be related to systematic changes in the internal microstructure of the material or the polymer topologies [10]. A graphical representation that is more amenable

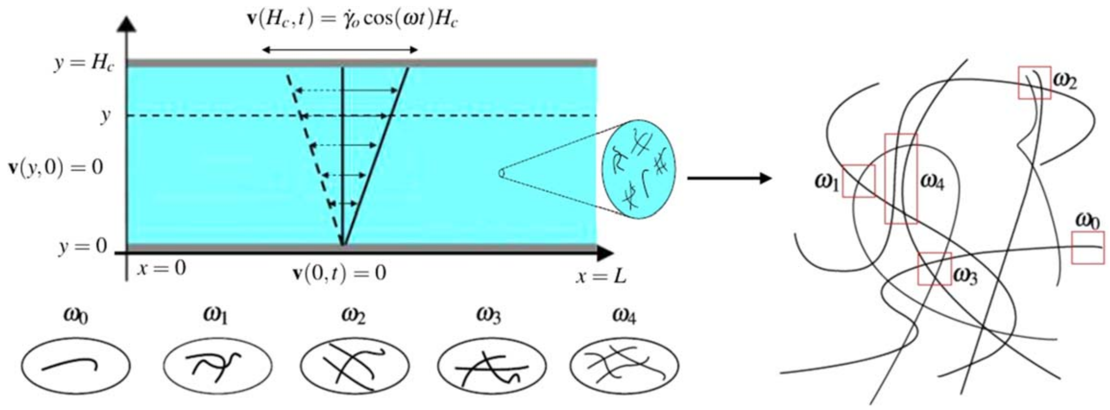

Figure 1. Schematic of the oscillatory shear flow and the transient network immersed in a Newtonian solvent indicating its microstates.

to rapid qualitative evaluation is the use of a closed loop plot or Lissajous curve (LC) of stress as a function of the strain or strain-rate [11]. This plot visually demonstrates how higher harmonic contributions, especially the third harmonic, can affect the measured output for a nonlinear viscoelastic material or complex fluid. There exists important information about the microstructure in the nonlinear regime, and LAOS experiments play an important role in revealing the interaction within complex fluids as well as in characterizing them [10].

There are different network models, which serve to determine the creation and destruction network functions. Sim *et al* investigated possible mechanisms of complex LAOS behavior using a network model composed of segments and junctions [12]. The classical transient network models consider creation to be a thermally activated process while the destruction of nodes is due to the flow force [13–15]. Rincón *et al* considered different entanglement scenarios was provided by the assumption of five microstates to describe transient network dynamics [16], where the rheological functions were calculated using the moments of the distribution function [17]. Ferrer *et al* [18] used the micro-macro approach to couple the Finitely Extensible Nonlinear Elastic (FENE) model with the transient network of Rincón *et al* [16] for a generalized complex fluid under simple shear flow.

Gómez-López *et al* performed numerical simulations of a FENE fluid under SAOS and LAOS using the Brownian Configuration Field Method (BCFM) [19]. It was found that the self-intersection in the LC produces secondary loops for short dumbbell extension lengths and a high ratio of dimensionless Weissenberg/Deborah numbers (Wi/De). The classical FENE model possesses a constant maximum length of extension [20]. Rincon *et al* [16] proposed a transient network model in which the extensibility is not a constant but a variable resulting from the creation and destruction processes, and the microstate dynamics is described by a kinetic process, which is a function of the available energy of the system as a result of flow or temperature.

In this paper, numerical simulations of complex fluids under SAOS and LAOS using a combined FENE transient network model is presented. The LC for the shear stress and the first normal stress difference with various kinetic rate constants versus the instantaneous strain-rate for viscoelastic projection are shown. The effect of Wi/De ratio, flow regime, variation of the forward and reverse kinetic rate constants is investigated and analyzed.The methodology developed in this paper through the consideration of the kinetics of microstrucural evolution will enable a greater understanding of the physics of complex fluids. It will also help to provide an interpretation of experimental data generated by SAOS and LAOS experiments to aid their characterization.

2. Transient network dynamics

The classical FENE dumbbell model, the maximum dumbbell extension is constant. To overcome this limitation, [16] considered a different way of modelling macromolecular interactions in terms of a transient network comprising a group of interconecting flexible chains, as shown in figure 1. The model system comprises nodes, which are points of physical interaction between two molecules, and segments, which are sections of the molecule between two nodes. A microstate is formed in terms of the number of nodes and describes the complexity of interactions amongst chains in a region of space. The topological configuration of the five basic microstates are shown in figure 1 and represented by a random arrangement of chains. A complex fluid involves the kinetics of creation and destruction of microstates, this process is called a transient network. It is possible to relate each microstate with its own relaxation time. The transient network has the ability to produce a spectrum of maximum extension lengths depending on the microstates immersed in the fluid. The microstates are created

Table 1. Properties of microstates.

Microstate	Number of nodes	Number of segments	Number of chains
ω_0	0	1	1
ω_1	1	4	2
ω_2	2	7	3
ω_3	3	9	3
ω_4	4	12	4

Table 2. Microstates properties.

Microstate	ν_i	τ_i	l_i
ω_0	$\frac{1}{4}$	1	1
ω_1	$\frac{1}{2}$	$\frac{1}{2}$	$\frac{1}{2}$
ω_2	$\frac{3}{4}$	$\frac{1}{3}$	$\frac{3}{7}$
ω_3	$\frac{3}{4}$	$\frac{1}{3}$	$\frac{1}{3}$
ω_4	1	$\frac{1}{4}$	$\frac{1}{3}$

by the molecular interaction, where structures that require less energy are favored. Hence, the microstates with lower energy correspond to those with the minimum number of interacting segments. The nomenclature used in the transient network model is as follows: ω_i represents a specific microstate where the subscript i indicates the number of nodes involved in a microstate. In this case, ω_0 is a single segment (free chain with no interactions) and ω_i, $i = 1, 2, 3, 4$ specifies the level of entanglement. In terms of average quantities, the maximum length of an extended free segment is defined by L_p and the maximum end-to-end distance between nodes in the network is $l'(t)$, which depends on time $t \in \mathbb{T}$. Rincón *et al* [16] show using conservation of chains that the time-dependent maximum extension length as a mapping l': $\mathbb{T} \to \mathbb{R}$; represented by (1):

$$l'(t) = \frac{VL_p(C_0 + 2C_1 + 3C_2 + 3C_3 + 4C_4)}{V(C_0 + 4C_1 + 7C_2 + 9C_3 + 12C_4)}, \tag{1}$$

where V and C_i are the volume occupied by the microstate and the concentrations of each microstate ω_i ($i = 0, 1, 2, 3, 4$), respectively. The dimensionless maximum length of extension time-dependent $l(t)$ is normalized, by dividing (1) by L_p to give

$$l(t) = \frac{l'(t)}{L_p} = \frac{C_0 + 2C_1 + 3C_2 + 3C_3 + 4C_4}{C_0 + 4C_1 + 7C_2 + 9C_3 + 12C_4}, \tag{2}$$

The numerator and denominator in (2) are the number of chains and number of segments in the network, respectively. The number of segments is defined in a similar way, noting that the concentration of segments includes the dangling ends. Table 1 characterizes the microstates in terms of nodes, the number of segments, and the number of chains, (for details see [16, 18]). Each microstate has its own extension length l_i, viscosity ν_i and time τ_i, which are determined:

$$\begin{aligned} l_i &= \frac{\text{individual microstate}}{\text{number of segments}}, \\ \nu_i &= \frac{\text{the simplest microstate}}{\text{number of microstates}}, \\ \tau_i &= \frac{\text{number of microstates}}{\text{the number of single microstates in the network.}} \end{aligned} \tag{3}$$

The characteristic maximum length of extension l_i for each microstate is shown in table 2 (column 4), that takes a particular value in the range $\frac{1}{3} \leqslant l_i \leqslant 1$. The properties of each microstate are based on the number of nodes, segments and microstates to form it, as shown in table 2. The maximum extension length, relaxation time and drag are different for each microstate.

2.1. Microstate kinetics

The transient network depends on the destruction/generation rate process of five different configurations (ω_i, for $i = 0, 1, 2, 3, 4$). The four different reversible processes that determine the destruction/generation rates of ω_i are represented by:

$$2\omega_0 \quad \underset{k_1^B \sigma : \mathbf{d}}{\overset{k_1^A \exp\left(-\frac{E_0}{KT}\right)}{\rightleftarrows}} \quad \omega_1, \tag{4}$$

$$3\omega_1 \quad \underset{k_2^B \sigma : \mathbf{d}}{\overset{k_2^A \exp\left(-\frac{E_0}{KT}\right)}{\rightleftarrows}} \quad 2\omega_2, \tag{5}$$

$$3\omega_1 + \omega_2 \quad \underset{k_3^B \sigma : \mathbf{d}}{\overset{k_3^A \exp\left(-\frac{4E_0}{KT}\right)}{\rightleftarrows}} \quad 3\omega_3, \tag{6}$$

$$2\omega_2 + 2\omega_3 \quad \underset{k_4^B \sigma : \mathbf{d}}{\overset{k_4^A \exp\left(-\frac{2E_0}{KT}\right)}{\rightleftarrows}} \quad 3\omega_4, \tag{7}$$

where k_i^A and k_i^B are the forward and backward rate constants ($i = 0, 1, 2, 3, 4$), respectively. The backward rate constants multiplied by the dissipation function $k_i^B \boldsymbol{\sigma}\colon \mathbf{d}$ is related to the process of breaking or changing of the transient network at a given time. In (4)–(7) E_0 is the characteristic interaction energy corresponding to form a single node, T is the temperature, K is the Boltzmann constant, $\boldsymbol{\sigma}$ is the total stress tensor, and $\mathbf{d}$ is the strain-rate tensor. The symmetric part of the strain-rate tensor is:

$$\mathbf{d} = \frac{1}{2}(\nabla \mathbf{v} + \nabla \mathbf{v}^T), \tag{8}$$

where $\mathbf{v}$ is the velocity field. In the first two transitions (4) and (5) the energy change represents E_0. For example, in the transition (5) three single-node configurations (six chains of energy content $3E_0$) result in two double-node configurations (six chains of energy content $4E_0$). For each transition, conservation of the chains is required. which explains why the simpler formation of ω_2 and ω_1 is not admissible (see (5)).

The simplified kinetic equations for destruction/generation of microstates are given in (9)–(13). The evolution of the microstate concentrations allows the determination of $l(t)$, where A (microstates generation) and B (microstates destruction or dissipative process) are the forward and backward kinetic rate constants, respectively. Forward rate constants are the quantities of structure formation, having Arrhenius temperature dependence [16], while the backward rate constants multiplied by the viscous dissipation function are the quantities of structure destruction.

$$\frac{dC_0}{dt} = B\ \boldsymbol{\sigma}\colon \mathbf{d}(C_1) - A(C_0^2), \tag{9}$$

$$\frac{dC_1}{dt} = B\ \boldsymbol{\sigma}\colon \mathbf{d}\left(-C_1 + C_2^2 + \frac{1}{4}C_3^3\right) + A\left(C_0^2 - C_1^3 - \frac{1}{4}C_1^3 C_2\right), \tag{10}$$

$$\frac{dC_2}{dt} = B\ \boldsymbol{\sigma}\colon \mathbf{d}\left(\frac{1}{4}C_3^3 + \frac{1}{2}C_4^3 - C_2^2\right) + A\left(C_1^3 - \frac{1}{4}C_1^3 C_2 - \frac{1}{2}C_2^2 C_3^2\right), \tag{11}$$

$$\frac{dC_3}{dt} = B\ \boldsymbol{\sigma}\colon \mathbf{d}\left(\frac{1}{2}C_4^3 - \frac{1}{4}C_3^3\right) + A\left(\frac{1}{4}C_1^3 C_2 - \frac{1}{2}C_2^2 C_3^2\right), \tag{12}$$

$$\frac{dC_4}{dt} = \frac{B}{2}\ \boldsymbol{\sigma}\colon \mathbf{d}(-C_4^3) + \frac{A}{2}(C_2^2 C_3^2). \tag{13}$$

3. Governing equations

This section presents the governing equations for solving viscoelastic flow problems using multiscale modeling. The equation system is related to macroscale, and the microscale to particle kinetics.

3.1. Macroscopic equations

The macroscopic equations comprise the conservation equations. The mathematical statement of the conservation of mass for an incompressible fluid is [29, 37]:

$$\nabla \cdot \mathbf{v} = 0, \tag{14}$$

while the Cauchy equation of motion (conservation of momentum) is [29, 37]:

$$\rho\left(\frac{\partial \mathbf{v}}{\partial t} + \mathbf{v} \cdot \nabla \mathbf{v}\right) = -\nabla p + \nabla \cdot \boldsymbol{\sigma}, \tag{15}$$

where p and ρ are pressure and fluid density. The stress tensor $\boldsymbol{\sigma}$ is defined as the sum of solvent and polymeric contributions, $\boldsymbol{\sigma}^s + \boldsymbol{\sigma}^p$, respectively.

$$\boldsymbol{\sigma} = \boldsymbol{\sigma}^s + \boldsymbol{\sigma}^p = 2\eta_s \mathbf{d} + \boldsymbol{\sigma}^p, \tag{16}$$

where η_s is the solvent viscosity. After describing the extra stress tensor, the momentum equation is:

$$\rho\left(\frac{\partial \mathbf{v}}{\partial t} + \mathbf{v} \cdot \nabla \mathbf{v}\right) = -\nabla p + \nabla \cdot \boldsymbol{\sigma}^p + \eta_s \nabla^2 \mathbf{v}. \tag{17}$$

3.2. Microscopic equations

In this paper, five different microstates are considered. The simplest microstate represents a single polymer chain and the FENE dumbbell model has been used for simulating macromolecules. An analysis based on rigid dumbbells was presented in Bird *et al* [21] and Schmalzer *et al* [22].

Polymer solutions are modeled as elastic dumbbell suspensions, in which the dumbbell is represented by two identical Brownian beads, with friction coefficient ζ, connected by a spring. The polymer solution is dilute so that the dumbbell interactions may be neglected. The configuration of a dumbbell is given in terms of a vector **Q** connecting the two beads of the dumbbell which provides information about the orientation and length of the spring (see figure 1). Considering the spring force, the viscous drag force and the force due to Brownian motion one can derive the equation of motion for the beads and hence the Fokker-Planck equation which [23], for homogeneous flows is:

$$\frac{\partial \psi}{\partial t} = -\frac{\partial}{\partial \mathbf{Q}}\left\{\left(\boldsymbol{\kappa}(t) \cdot \mathbf{Q} - \frac{2}{\zeta}\mathbf{F}\right)\psi\right\} + \frac{2kT}{\zeta}\frac{\partial}{\partial \mathbf{Q}}\frac{\partial}{\partial \mathbf{Q}}\psi, \tag{18}$$

where $\boldsymbol{\kappa}$ is the velocity gradient, T is absolute temperature, k is Boltzmann's constant and $\mathbf{F}(\mathbf{Q})$ is the spring force. The solution of (18) furnishes the probability $\psi(\mathbf{Q}, \mathbf{x}, t)d\mathbf{Q}$ of finding a dumbbell with configuration in the range $\mathbf{Q}$ to $\mathbf{Q} + d\mathbf{Q}$ at $(\mathbf{x}, t)$. Once the configuration probability density function (pdf), ψ, is known the polymeric contribution to the extra-stress may be determined with the Kramers expression

$$\boldsymbol{\sigma}^{\mathbf{p}} = -nkT\mathbf{I} + n\langle \mathbf{Q} \otimes \mathbf{F}(\mathbf{Q})\rangle, \tag{19}$$

where n is the number of polymer molecules per unit volume, the symbol $\otimes$denotes the outer product of two vectors and the angular brackets denote the ensemble average over configuration space.

The spring force for Hookean dumbbells is defined as:

$$\mathbf{F}(\mathbf{Q}) = H\mathbf{Q}, \tag{20}$$

where H is the spring constant. Note that this linear spring law performs well in weak field flows, in which the chain is close to its equilibrium state, as described in [17, 24]. This law has a problem, at high flow rates and in extensional flow, the chains extend without limit, but the real polymers can only extend, at most, to their fully stretched length, as long as they do not break. Warner proposed the FENE spring law to adress this restriction [20]:

$$\mathbf{F}(\mathbf{Q}) = \frac{H\mathbf{Q}}{1 - (\mathbf{Q}/Q_0)^2}, \tag{21}$$

where Q_o is the maximum extension length of a single spring, for long chains it is equivalent to a Hookean dumbbell. The solution of (18), is unfortunately not always possible, particularly with many particle systems, but there exists an equivalence between equation (18) and a stochastic partial differential equation (SPDE) [23, 25, 26]:

$$d\mathbf{Q}(t) = \left(\boldsymbol{\kappa}(t) \cdot \mathbf{Q} - \frac{2}{\zeta}\mathbf{F}\right)dt + \sqrt{\frac{4kT}{\zeta}}\, d\boldsymbol{\Phi}. \tag{22}$$

In this SPDE, the term $\boldsymbol{\Phi}$ represents a multi-dimensional Wiener process and its corresponding scale is $\sqrt{t}$ [26, 27]. The connector vector length **Q** is scaled by $\sqrt{kT/H}$. If we define the relaxation time and polymeric viscosity by

$$\lambda = \frac{\zeta}{4H}, \quad \eta_p = nkT\lambda.$$

one can derive the Oldroyd B model in the case of Hookean dumbbells, where n is the number of molecules per unit of volume in the system. This provides the link between the macroscopic and microscopic contributions. The maximum extension length Q_o and λ characterize the microstructure.

BCFM considers the multiscale contribution of viscoelastic fluids problems [25, 28–30]. A configuration field approach is used to reduce the variance by introducing a convective term in (22):

$$d\mathbf{Q}(t) = \left(-\mathbf{v}\cdot\nabla\mathbf{Q} + \boldsymbol{\kappa}(t)\cdot\mathbf{Q} - \frac{1}{2\lambda}\mathbf{F}(\mathbf{Q})\right)dt + \sqrt{\frac{1}{\lambda}}\,d\boldsymbol{\Phi}(t). \tag{23}$$

After calculating the spatial configuration field, the polymeric stress can be determined by the Kramers expression (19), by using η_p and λ [17, 31]:that is then used in the momentum equation to calculate the new velocity field. To evaluate the individual contribution of each microstate, (23) and (24) are generalized as follows:

$$d\mathbf{Q}_i(t) = \left(-\mathbf{v}\cdot\nabla\mathbf{Q}_i + \boldsymbol{\kappa}(t)\cdot\mathbf{Q}_i - \frac{1}{2\lambda_i}\mathbf{F}_i(\mathbf{Q}_i)\right)dt + \sqrt{\frac{1}{\lambda_i}}\,d\boldsymbol{\Phi}_i(t), \tag{25}$$

$$\boldsymbol{\sigma}_i = \frac{\eta_i}{\lambda_i}(-\mathbf{I} + \langle \mathbf{Q}_i \otimes \mathbf{F}_i(\mathbf{Q}_i)\rangle), \tag{26}$$

where

$$\mathbf{F}_i(\mathbf{Q}_i) = \frac{H\mathbf{Q}_i}{1 - (\mathbf{Q}_i/l_i Q_0)^2}, \tag{27}$$

and l_i is a extension length scale factor for each microstate described in table 2. The polymeric stress contribution is defined as:

$$\boldsymbol{\sigma}^p = \sum_{i=0}^{4}\boldsymbol{\sigma}_i, \tag{28}$$

with $\lambda_i = \tau_i\lambda$, $\eta_i = C_i\nu_i n k_b T\lambda_i$.

4. Dimensionless equations

The governing equations are made dimensionless using the following non-dimensional variables

$$\boldsymbol{x}^* = \frac{\mathbf{x}}{H_c},\quad \mathbf{v}^* = \frac{\mathbf{v}}{\dot{\gamma}_0 H_c},\quad t^* = \omega t,\quad \boldsymbol{\sigma}^{p*} = \frac{\sigma^p}{\eta_0\dot{\gamma}_0},\quad \dot{\gamma}^* = \dot{\gamma}\dot{\gamma}_0, \tag{29}$$

where $\mathbf{x}$ is the position vector, $\mathbf{v}$ is the velocity vector, t is time, $\boldsymbol{\sigma}^p$ is the polymeric contribution to the extra stress tensor, $\dot{\gamma}$ is the strain-rate tensor, H_c is a characteristic length scale which in this paper is the distance between the parallel plates and η_0 is the zero-shear-rate viscosity. The velocity is $\mathbf{v} = (u, 0, 0)$ where u is the velocity vector component in x-direction, defined by $u(y,\ t) = \dot{\gamma}_0\cos(\omega t)y$. The corresponding initial and boundary conditions are $u(y, 0) = 0$, $u(H_c,\ t) = \dot{\gamma}_0\cos(\omega t)H_c$, respectively.

With this choice of non-dimensional variables the momentum equation becomes

$$\frac{ReDe}{Wi}\frac{\partial\mathbf{v}^*}{\partial t^*} = \beta\nabla^{*2}\mathbf{v}^* + \nabla^*\cdot\boldsymbol{\sigma}^{p*}, \tag{30}$$

where Re and $\beta = \eta_s/\eta_0$ are the Reynolds number and the viscosity ratio, respectively. The total viscosity is defined by $\eta_0 = \eta_s + \eta_p$, where η_p is the zero-shear-rate polymer viscosity. The dimensionless initial and boundary conditions are $u^*(y, 0) = 0$, $u^*(0, t^*) = 0$ and $u^*(1,\ t^*) = \cos(t^*)$.

Regarding the microscopic equations, the vectors $\mathbf{Q}$ and $\boldsymbol{\Phi}$ are scaled with $\sqrt{kT/H}$ and $\sqrt{\frac{1}{\omega}}$, respectively.

$$d\mathbf{Q}^* = \left(-\frac{Wi}{De}\mathbf{v}^*\cdot\nabla^*\mathbf{Q}^* + \frac{Wi}{De}\boldsymbol{\kappa}^*(t)\cdot\mathbf{Q}^* - \frac{1}{2De}\mathbf{F}(\mathbf{Q}^*)\right)dt^* + \sqrt{\frac{1}{De}}\,d\mathbf{W}, \tag{31}$$

The dimensionless polymeric stress is given by the Kramers expression:

$$\boldsymbol{\sigma}_i^{p*} = \alpha_{b,d}\frac{C_i\nu_i(1-\beta)}{Wi}(\langle\mathbf{Q}_i^*\otimes\boldsymbol{F}_i(\mathbf{Q}_i^*)\rangle - \boldsymbol{I}), \tag{32}$$

where

$$\alpha_{b,d} = \begin{cases} 1,\text{Hookean}, \\ \frac{b+d+2}{b},\text{FENE}, \end{cases} \tag{33}$$

where d denotes the dimension of the problem, $\mathbf{Q}^*$ is the dimensionless configuration vector and $\mathbf{W}$ is the Wiener process. In this paper, $d = 2$ and $\mathbf{F}(\mathbf{Q}^*)$ is:

$$\mathbf{F} = \frac{\mathbf{Q}^*}{1 - (\mathbf{Q}^{*2}/b)}. \tag{34}$$

where $b = HQ_0^2/kT$ is the dimensionless maximum extension length, so that when $b \to \infty$ the spring behaves as a Hookean dumbbell. The dimensionless form of the individual microstate SDEs are:

$$d\mathbf{Q}_i^* = \left(-\frac{Wi}{De}\mathbf{v}^* \cdot \nabla^*\mathbf{Q}_i^* + \frac{Wi}{De}\boldsymbol{\kappa}^* \cdot \mathbf{Q}_i^* - \frac{1}{2\tau_i De}\mathbf{F}_i(\mathbf{Q}_i^*)\right)dt^* + \sqrt{\frac{1}{\tau_i De}}\,d\mathbf{W}_i, \tag{35}$$

where

$$\mathbf{F}_i(\mathbf{Q}_i^*) = \frac{H\mathbf{Q}_i^*}{1 - \left(\frac{\mathbf{Q}_i^* \cdot \mathbf{Q}_i^*}{l_i^2 b}\right)}, \tag{36}$$

$$\alpha_i = \frac{l_i^2 b + d + 2}{l_i^2 b} \tag{37}$$

and corresponding Kramers expression

$$\boldsymbol{\sigma}^{p*} = \sum_{i=0}^{n} C_i \alpha_i \frac{\nu_i(1-\beta)}{Wi}(\langle \mathbf{Q}_i^* \otimes \mathbf{F}_i(\mathbf{Q}_i^*)\rangle - \mathbf{I}). \tag{38}$$

5. Numerical solution

The numerical solution for solving under SAOS and LAOS conditions of complex fluids with transient network dynamics is presented. A decoupled micro-macro numerical scheme is used [19]. In the macroscopic part of the numerical scheme, the velocity and pressure are determined at the new time level by solving the conservation equations for a given polymeric contribution to the extra-stress tensor. The new velocity field is then used as an input to the microscopic part of the numerical scheme in which the polymeric contribution to the extra-stress tensor is determined at the same time level. This process is repeated until a steady state or periodic solution is obtained.

The same numerical scheme developed by [19], employing finite differences to discretize the system of governing equations, is used. The computational space is $\Omega \times \mathbb{T}$ where Ω is defined by $C \times D \coloneqq \{(x, y) | x \in C, y \in D\}$ and $\mathbb{T} \in \mathbb{R}$ is the time interval. In this paper $C = [0, 10]$, $D = [0, 20]$ and $\mathbb{T} = [0, t_{\max}]$, where $t_{\max}$ is the periodic or steady-state dimensionless time [18, 32].

The momentum equation is solved using an implicit iterative ADI method [32]. For the temporal and spatial derivatives, forward and central difference discretizations are used, respectively. For the polymeric extra-stress a semi-implicit predictor-corrector scheme is used:

$$\begin{aligned}\tilde{\mathbf{Q}}_k^{n+1} = \mathbf{Q}_k^n &+ \left(-\frac{Wi}{De}\mathbf{v}^n \cdot \nabla\mathbf{Q}_k^n + \frac{Wi}{De}\nabla\mathbf{v}^n \cdot \mathbf{Q}_k^n - \frac{1}{2De}\mathbf{F}(\mathbf{Q}_k^n)\right)\Delta t \\ &+ \sqrt{\frac{1}{De}}\mathbf{W},\end{aligned} \tag{39}$$

$$\begin{aligned}\left(1 + \frac{\Delta t}{4De}\mathbf{F}(\tilde{\mathbf{Q}}_k^{n+1})\right)\mathbf{Q}_k^{n+1} &= \mathbf{Q}_k^n - \frac{1}{2}\frac{Wi}{De}(\mathbf{v}^n \cdot \nabla\mathbf{Q}_k^n + \mathbf{v}^n \cdot \nabla\tilde{\mathbf{Q}}_k^{n+1}) \\ &+ \frac{1}{2}\frac{Wi}{De}(\nabla\mathbf{v}_k^n \cdot \mathbf{Q}_k^n + \nabla\mathbf{v}_k^n \cdot \tilde{\mathbf{Q}}_k^{n+1}) \\ &+ \frac{\Delta t}{4De}\mathbf{F}(\mathbf{Q}_k^n) + \sqrt{\frac{1}{De}}\mathbf{W}.\end{aligned} \tag{40}$$

The predictor step (39) is used to determine $\tilde{\mathbf{Q}}_k^{n+1}$, before the corrector step (40) is used to evaluate $\mathbf{Q}$ at the next time step [30, 31, 33].

The polymeric contribution to the extra-stress is determined using a discrete version of the Kramers expression (38)

$$\boldsymbol{\sigma}^p = \alpha_{b,d}\frac{(1-\beta)}{Wi}\left(-\mathbf{I} + \frac{1}{N_f}\sum_{k=1}^{N_f}\mathbf{Q}_k^{n+1} \otimes \mathbf{F}(\mathbf{Q}_k^{n+1})\right), \tag{41}$$

where N_f defines the number of Brownian configuration fields. For information on statistical error as well as numerical convergence, see [31]. The time step $\Delta t = 0.001$ is used in all of the simulations. Full details of the algorithm can be found in [18, 19].

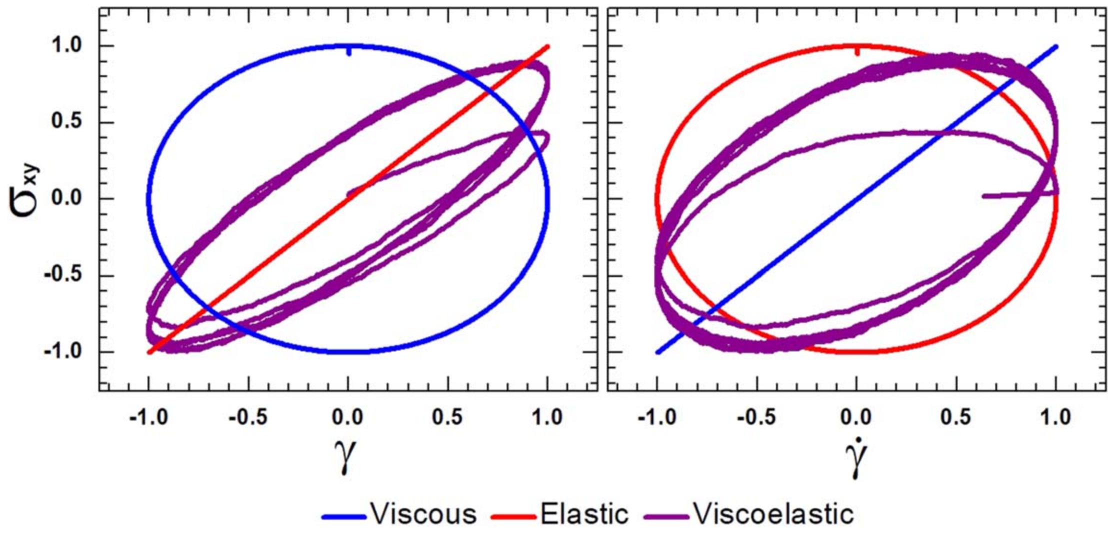

Figure 2. Lissajous curves: elastic form (σ_{xy} versus γ) (left) and viscous form (σ_{xy} versus $\dot{\gamma}$) (right) with $Wi/De = 1, b = 50, A = 1, B = 1, Re = 0.001$ and $N_f = 1500$.

6. SAOS and LAOS characterization

The description of the problem consists of a complex fluid enclosed between two infinite parallel plates, spaced by a distance H_c. The lower plate is stationary for all time. The upper plate is at rest for $t \leqslant 0$ while for $t > 0$ it begins an oscillatory motion of small or large amplitude, as presented in figure 1. The fluid is an incompressible dilute polymeric solution. To analyze the fluid behavior, the LC is widely used for both SAOS and LAOS tests [6, 21, 22, 34–36].

The LC are plots of the instantaneous stress versus strain or strain rate, elastic or viscous projection, respectively. For SAOS regime, the stress response is linear, the input and the output signals are in-phase, out-phase or the input is shifted by a certain angle δ. For elastic solids, the LC is a straight line, for viscous fluids a circular orbit and for viscoelastic fluids a tilted ellipse in the elastic projection, respectively [37]. The LC of the elastic and viscous projections are shown in figure 2. In the LAOS regime, the stress response is nonlinear, and the LC for a viscoelastic fluid departs from the elliptical shape found in the SAOS regime in many different ways. Researchers have focused on characterizing the nonlinear stress response through different methods. More information on this is available in several publications [1, 36, 37]. In this paper, a complex fluid under SAOS and LAOS regime is characterized by using sinusoidal shear $\gamma_{xy} = \gamma_0 \sin(\omega t)$ with strain-rate $\dot{\gamma}_{xy} = \dot{\gamma}_0 \cos(\omega t)$, where t, γ_0 and ω are time, strain amplitude and oscillation frequency, respectively [36], where $\dot{\gamma}_0 = \gamma_0\omega$. Utilizing the characteristic relaxation time of the fluid, the dimensionless strain-rate is expressed as:

$$\lambda\dot{\gamma}_{xy} = \lambda\dot{\gamma}_0 \cos\left(\omega\lambda\frac{t}{\lambda}\right) = Wi \cos\left(De\frac{t}{\lambda}\right) \tag{42}$$

where $De = \lambda\omega$ and $Wi = \lambda\dot{\gamma}_0$ represent the dimensionless Deborah and Weissenberg numbers, respectively. As mentioned by a number of researchers [21, 22, 36], the relationship between De and Wi in (42) is used to define the LAOS regime for a viscoelastic material. A modification of De or Wi deviates the fluid response from Newtonian behavior. This behavior is described by the complex number $Gn = De + iWi$, with magnitude defined by $|Gn| = \sqrt{De^2 + Wi^2}$ and corresponding angle by $\hat{\phi} = \arctan\left(\frac{Wi}{De}\right)$, according to the criteria proposed by [36]. This analysis has two purposes. First to establish guidelines for the identification of the flow conditions for the LAOS $\left(\frac{Wi}{De} \geqslant 1\right)$ and SAOS regimes $\left(\frac{Wi}{De} < 1\right)$ or the case of simple shear $\left(\hat{\phi} = \frac{\pi}{2}\right)$. It also provides a tool for analyzing different time scales.

7. Results

The results for SAOS and LAOS tests of a complex fluid are obtained by using the scheme described in section 5 and programmed in Fortran. The numerical code validation was performed by comparing the Oldroyd-B and Hookean dumbbell models in a simple shear flow. A comprehensive description of the numerical algorithm can be found in a previous publication of the authors [19].

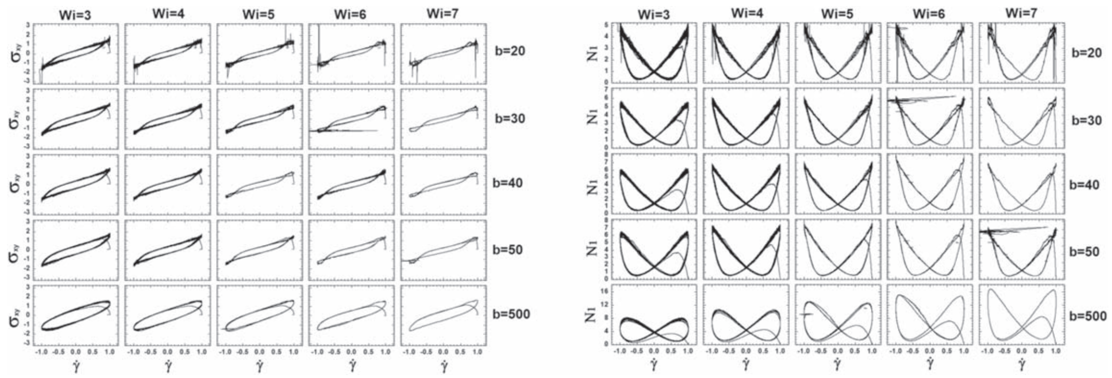

Figure 3. Lissajous curves for σ_{xy} (left) and N_1 (right) versus $\dot{\gamma}$ for different *Wi* and *b* with $De = 1$, $\beta = 0.1$, $Re = 0.001$ and $N_f = 1500$.

7.1. Numerical simulation predictions

In this section, the evolution of concentrations and Lissajous plots are used to analyze the effect of the main variables (b, β, Wi, De and Wi/De ratio) of the model on complex fluid behavior. Elastic and viscous projections in Lissajous plots of a complex fluid under SAOS and LAOS conditions for σ_{xy} and N_1 versus γ_{xy} or $\dot{\gamma}_{xy}$ is performed, where N_1 is defined by $N_1 = \sigma_{xx} - \sigma_{yy}$. Starting with the same kinetic scheme used in previous work [19], figure 3 presents the viscous projection of the shear stress σ_{xy} and N_1 for different values of Wi/De and b under LAOS regime. By increasing the maximum extension length, no relevant changes in σ_{xy} were found. However, the magnitude of N_1 increases as Wi is increased. It is well known that the Hookean and FENE models are equivalent under these conditions. An important finding of the FENE model is to identify the conditions when self-intersections appear in the Lissajous plots, which are for large Wi/De values and short chain lengths. Similar predictions were reported by [38] who quantified the LAOS dynamics of the Giesekus constitutive model at large Wi via singular perturbation methods. The viscous LC exhibited a secondary loop while the elastic LC was a straight line with negative slope.These findings were consistent with the experiments of [39] on wormlike micelle solutions whose shear rheology closely follows a single-mode Giesekus model. Férec *et al* used SAOS and LAOS measurements to investigate the rheological behavior of short glass fibers suspended in polybutene and molten polypropylene [40]. They determined material functions such as shear stress and primary normal stress differences from the raw signals using a parallel plate rheometer. For suspensions based on polybutene, the shear stress amplitude grows with increasing cycles of deformation to reach a constant value after more than 20 cycles. The opposite behavior, i.e. a decrease of the shear stress amplitude, was observed for the polypropylene composites. For both filled systems the evolution was attributed to fiber orientation under flow, with the differences in behavior caused by different initial fiber orientations.

7.2. Comparison of kinetic schemes

The kinetics of microstates is analogous to chemical kinetics, and describes the physical interaction of macromolecules immersed in a Newtonian solvent, in which the microstates are defined by the number of nodes. Molecular collisions involve a Brownian diffusion process, as well as the formation of physical entanglements that require a specific state of thermal energy to form a node. Under flow, the number of nodes decreases because the deformation energy exceeds the interaction energy between the molecules participating in a node.

In this section, two kinetic schemes are compared. The first scheme (Kinetics 1) is the one used by Ferrer *et al* [18] for the transient network model under simple shear flow using BCFM, where N_f is the number of trajectories or configuration fields in the whole system. The second scheme (Kinetics 2), coupling the transient network model, comprises five microstates where each microstate uses N_f configuration fields in order to determine its extension length. The simplest microstate ω_0 is equivalent to a FENE dumbbell. Therefore the computational cost of the second scheme is higher.

A comparison of the microstate concentration evolution for weakly and highly structured networks using the two kinetic schemes is shown in figure 4. Note that the oscillating behavior is due to the imposed oscillatory shear flow (see (42)). This is responsible for the cyclical nature of the creation/destruction of microstructures. Both kinetic schemes exhibit the same time evolution with small changes in magnitude. Figure 5 presents the effect of the kinetic rate constants A and B on the LC for the viscous projection of the shear stress σ_{xy}, from a weakly ($A = 1, B = 100$) to a highly ($A = 100, B = 1$) structured network. For both kinetic schemes nonlinear behavior is observed. The shape and magnitude of the LC are modified using Kinetics 2 while for Kinetics 1 no change is seen. Kinetics 2 is used for all subsequent simulations.

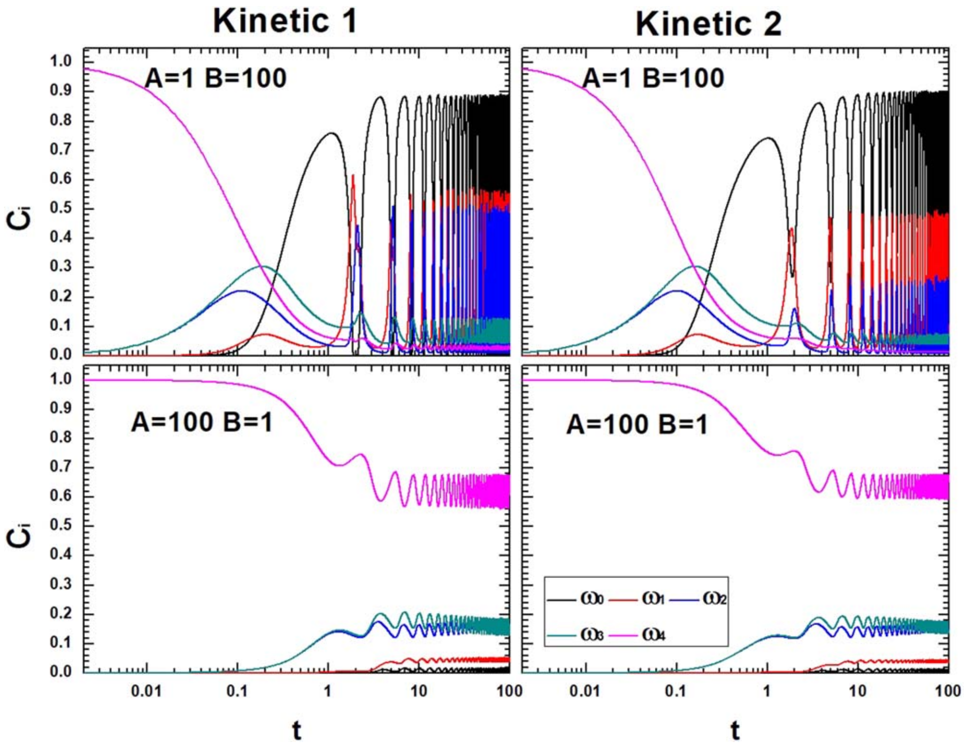

Figure 4. Time evolution of microstate concentrations for disentanglement ($A = 1$ and $B = 100$) and entanglement ($A = 100$ and $B = 1$) structured network using two different kinetic schemes with $Wi/De = 5$, $De = 1$, $\beta = 0.1$, $b = 50$, $Re = 0.001$ and $N_f = 1500$.

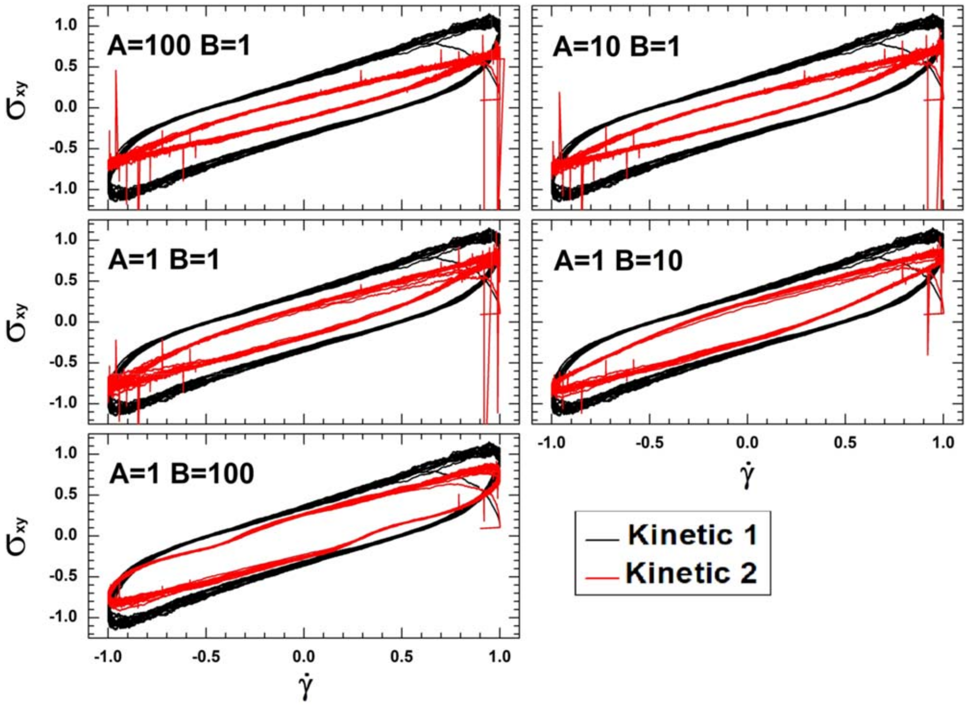

Figure 5. Effect of the kinetic rate constants A and B on the Lissajous curves using two kinetic schemes with $Wi/De = 5$, $De = 1$, $\beta = 0.1$, $b = 50$, $Re = 0.001$ and $N_f = 1500$.

7.3. Viscosity ratio β

Figure 6 presents the influence of the viscosity ratio β on the time evolution of the microstate concentrations for three different initial structured networks: (i) disentanglement, only free chains, microstate ω_0, (ii) entanglement, only microstate ω_4 defined by four chains, and (iii) aleatory, all the microstates are present. The

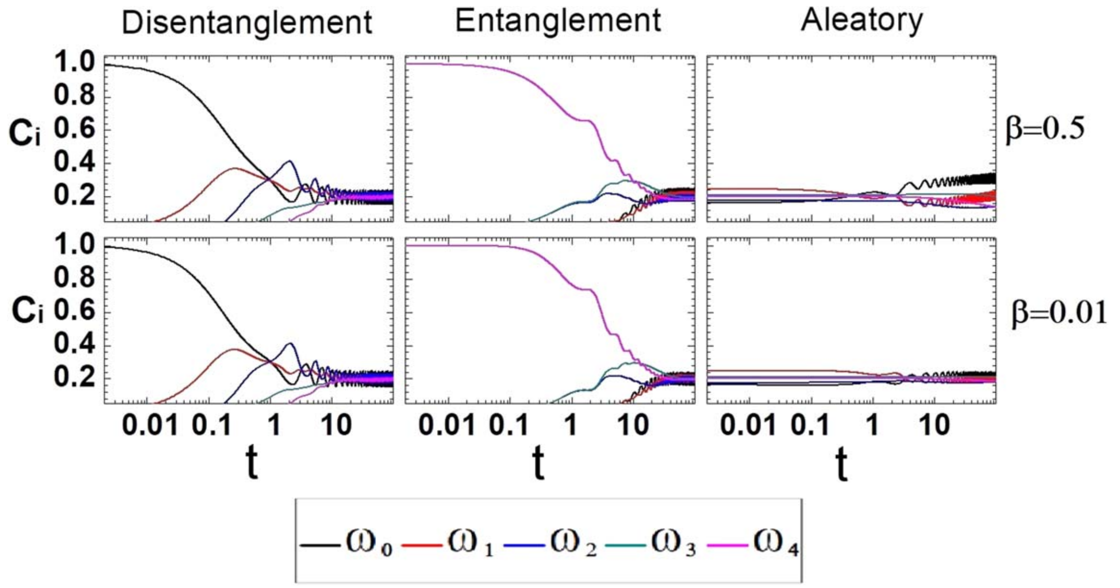

Figure 6. Influence of the viscosity ratio β on the time evolution of microstate concentrations for different initial conditions with $Wi/De = 1$, $De = 1$, $b = 50$, $A = 1$, $B = 1$, $Re = 0.001$ and $N_f = 1500$.

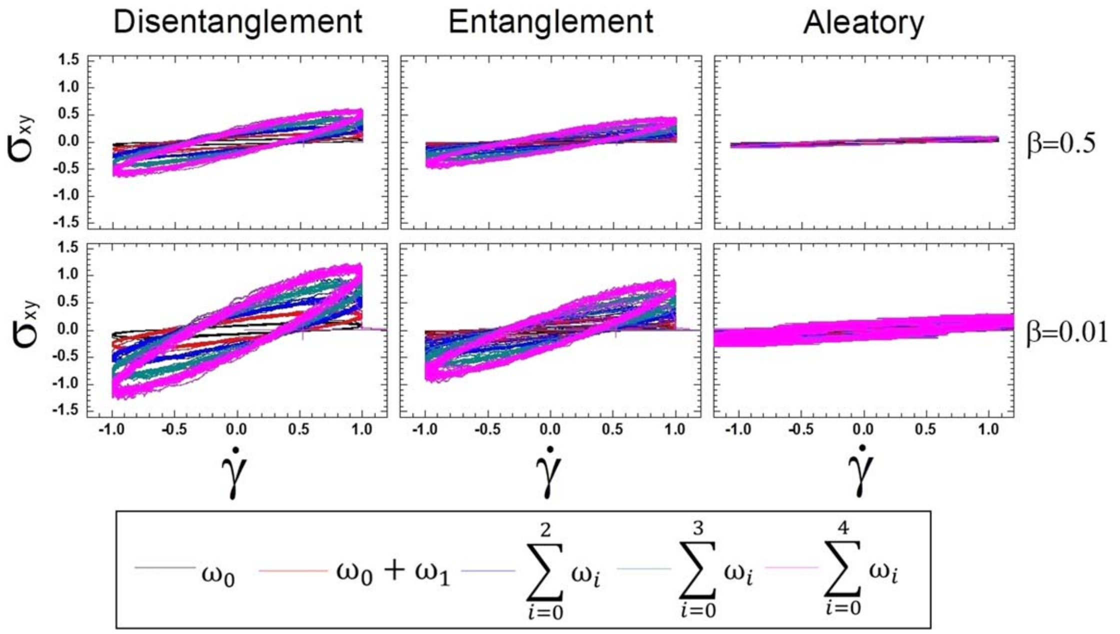

Figure 7. Influence of the viscosity ratio β on the Lissajous curves for different initial concentrations with $Wi/De = 1$, $De = 1$, $b = 50$, $A = 1$, $B = 1$, $Re = 0.001$ and $N_f = 1500$.

initial microstate concentration conditions are: disentanglement ($\omega_0 = 1$, and $\omega_i = 0$ for $i = 1, 2, 3, 4$), entanglement ($\omega_4 = 1$, and $\omega_i = 0$ for $i = 0, 1, 2, 3$), and aleatory structured network ($\omega_i \neq 0$ for $i = 0, 1, 2, 3, 4$). The initial entanglement scenario of a transient network is a function of the system's available energy. This energy depends on the flow condition and is quantified through viscous dissipation. The influence of β on all the entanglement scenarios is shown to slightly modify the microstate concentration values. It is important to note the aleatory case with $\beta = 0.5$, generates an increase of the microstates ω_0 and ω_1 which is correct because the system gives preference to the formation of microstates with lower energy requirements.

Figure 7 exhibits the effect of β on the LC of the individual shear stress σ_{xy} associated with each microstate for different initial entanglement scenarios. The number of microstates is implicit in the polymer viscosity contribution. In this case lower values of β correspond to a viscoelastic fluid and higher values to a viscous fluid.

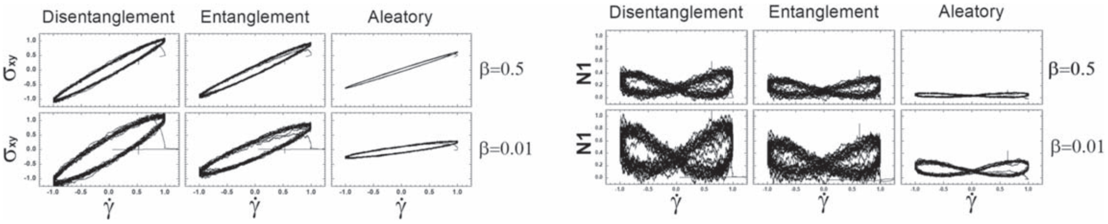

Figure 8. Influence of the viscosity ratio β on the Lissajous curves for σ_{xy} (left) and N_1 (right) versus $\dot{\gamma}$ with different entanglement scenarios with $Wi/De = 1$, $b = 50$, $A = 1$, $B = 1$, $Re = 0.001$ and $N_f = 1500$.

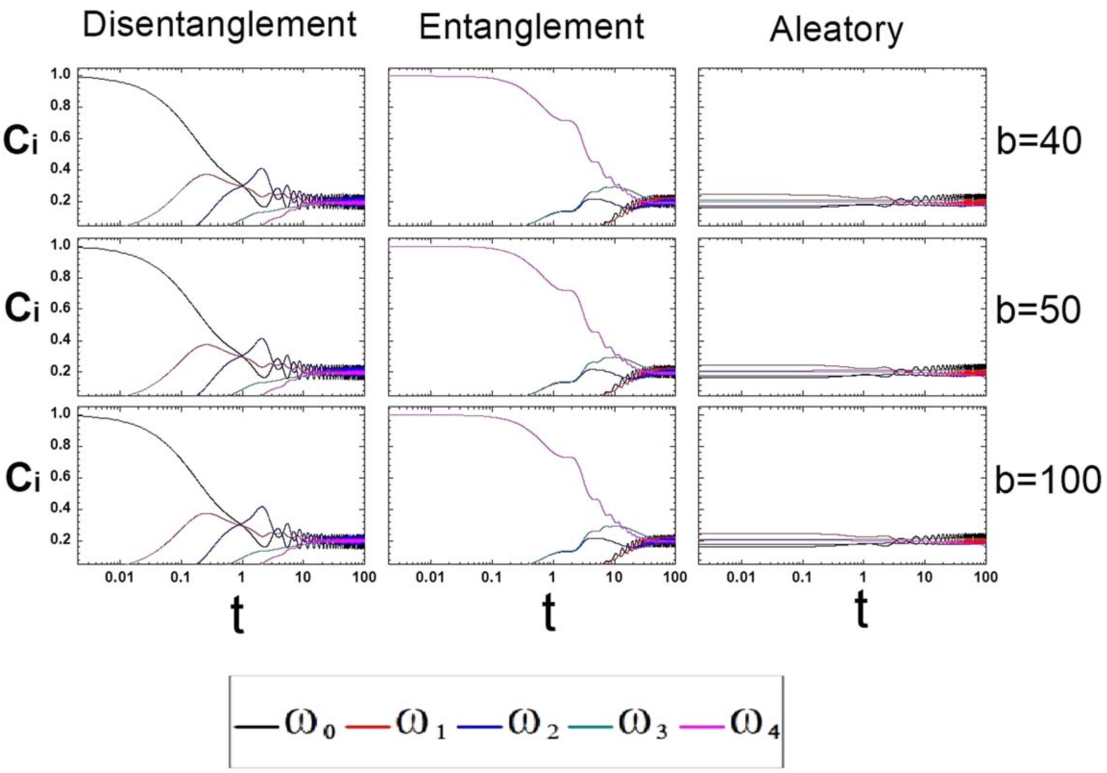

Figure 9. Influence of the extension length b on the time evolution of microstate concentrations with different entanglement scenarios with $Wi/De = 1$, $De = 1$, $\beta = 0.1$, $A = 1$, $B = 1$, $Re = 0.001$ and $N_f = 1500$.

In this figure decreasing β increases the σ_{xy} microstate magnitudes. This effect can be better appreciated in the total shear stress and its corresponding first normal stress difference N_1 which are shown in figure 8.

7.4. Extension length *b*

An important characteristic of this work with respect to the literature is that it facilitates coupling the FENE and transitory network models [18, 19]. In the classical FENE model (see (34)) b is a constant. The transient network model allows us to generalise this by associating a maximum extension length to each of the five basic microstates using a scale factor l_i shown in table 2 [16]. The maximum extension length b corresponds to microstate ω_0. Figure 9 shows the effect of b on the time evolution of microstate concentrations with different entanglement scenarios under SAOS flow. The microstate concentrations are affected when $b = 40$, mainly ω_0 and ω_1 which are more sensitive to energetic changes of the transitory network. For larger values of b there are no significant changes in concentrations. Figure 10 presents the effect of the extension length b on the LC for each shear stress σ_{xy} for different entanglement scenarios. All curves have the characteristic elliptical shape corresponding to SAOS regime. Note that some noise is generated in the curves shown for short extension lengths ($b = 40$). In order to complement these numerical predictions with experiments, Anvari and Joyner characterized the effects of concentrated emulsions as a fat replacer on the viscoelastic properties of reduced-fat (15 % fat) and low-fat (6% fat) Cheddar cheeses under SAOS and LAOS flow [41]. They reported the LC of cheeses at different fat contents and storage timepoints. The shape of the LC for all samples was elliptical at

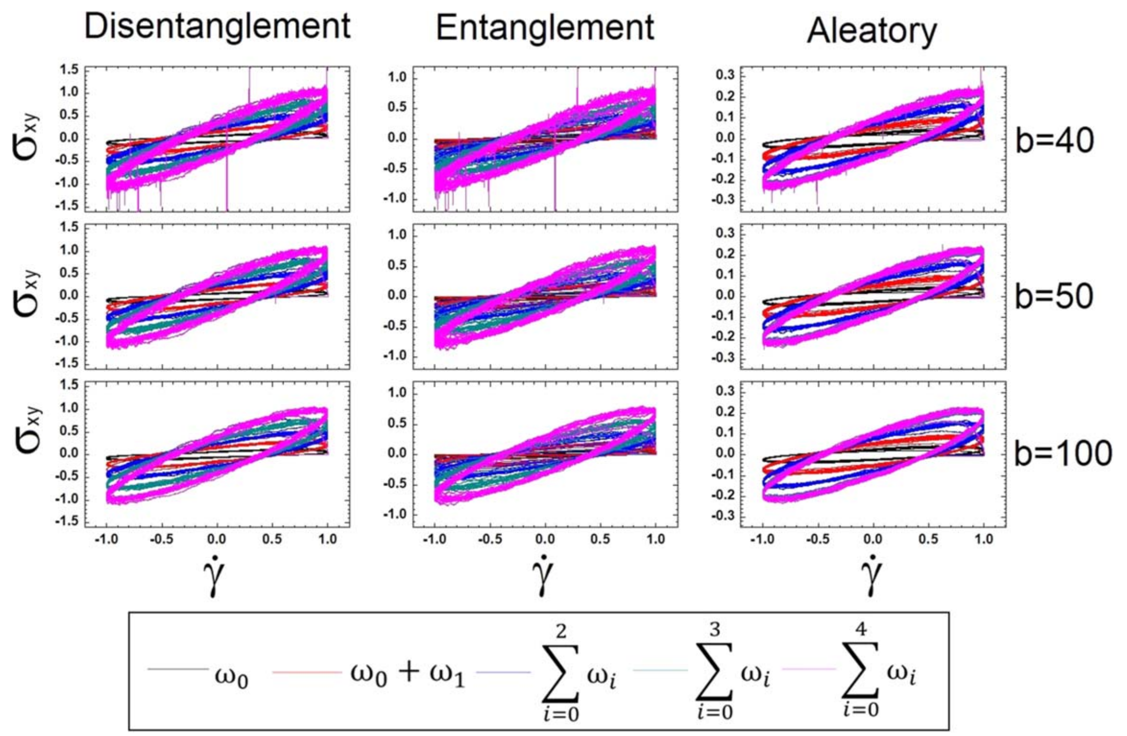

Figure 10. Influence of the extension length b on the Lissajous curves for each shear stress σ_{xy} for different entanglement scenarios with $Wi/De = 1$, $De = 1$, $\beta = 0.1$, $A = 1$, $B = 1$, $Re = 0.001$ and $N_f = 1500$.

0.05% strain (linear regime), indicating ideal viscoelastic behavior. Under higher strains, nonlinearities were presented as a distortion from the elliptical shape. Specific distortions of the shapes were related to different microstructural features.

7.5. Influence of *Wi*

Figure 11 presents the influence of the Weissenberg number Wi on the time evolution of microstate concentrations for different entanglement scenarios. The microstate concentrations do not show significant changes when the Wi value is changed. Figures 12–14 show the effect of Wi on the LC for the shear stress σ_{xy} and the first stress difference N_1 for each microstate with different entanglement scenarios under LAOS regime. In order to analyze only the Wi effects, the parameter values selected for these cases are $b = 50$, $A = 1$ and $B = 1$, while the generation and destruction of microstates are the same. Starting with a disentanglement network, increasing Wi the elliptical shape of the shear stress is lost, and the formation of small secondary loops for each microstate are found in the total shear stress only for $Wi = 7$. N_1 mainly changes in magnitude. In the entanglement network, thixotropic behavior can be seen in the shear stress and N_1, due to the microstructual evolution of the transitory network and convergence is lost at values greater than $Wi = 6$. In the aleatory network, there is a loss of the elliptical shape of the shear stress. Also thixotropic behavior can be observed in the shear stress and N_1 when $Wi \geqslant 6$ and only for the microstates ω_0 and ω_1. Tong *et al* investigated the rheological properties of gellan fluid gels using the LAOS technique, with consideration of high acyl (HA)/low acyl (LA) gellan ratio and Ca^{2+} concentration [42]. LC and Chebyshev coefficients were used to analyze the LAOS data and this was successful in visually and quantitatively representing the microstructural differences between HA and LA gellan gum, respectively. For small strain amplitude, the viscous LC produced an elliptical shape for all Ca^{2+} concentrations. With increasing strain amplitude, the LC adopted complex shapes and secondary loops corresponding to self-intersection and strong nonlinear elastic responses appeared.

7.6. Influence of the kinetic rate constants *A* and *B*

Figure 15 presents the effect of the kinetic rate constants A and B on the time evolution of microstate concentrations for different entanglement scenarios. As expected, modifying A and B the microstate concentrations has a direct impact on the rate change of the build-up and break-up processes. It is important to note that the effect of the kinetic constants favors the formation of a structured network or the destruction of the same, but as the transitory network evolves, it gives preference to form microstates with lower energy

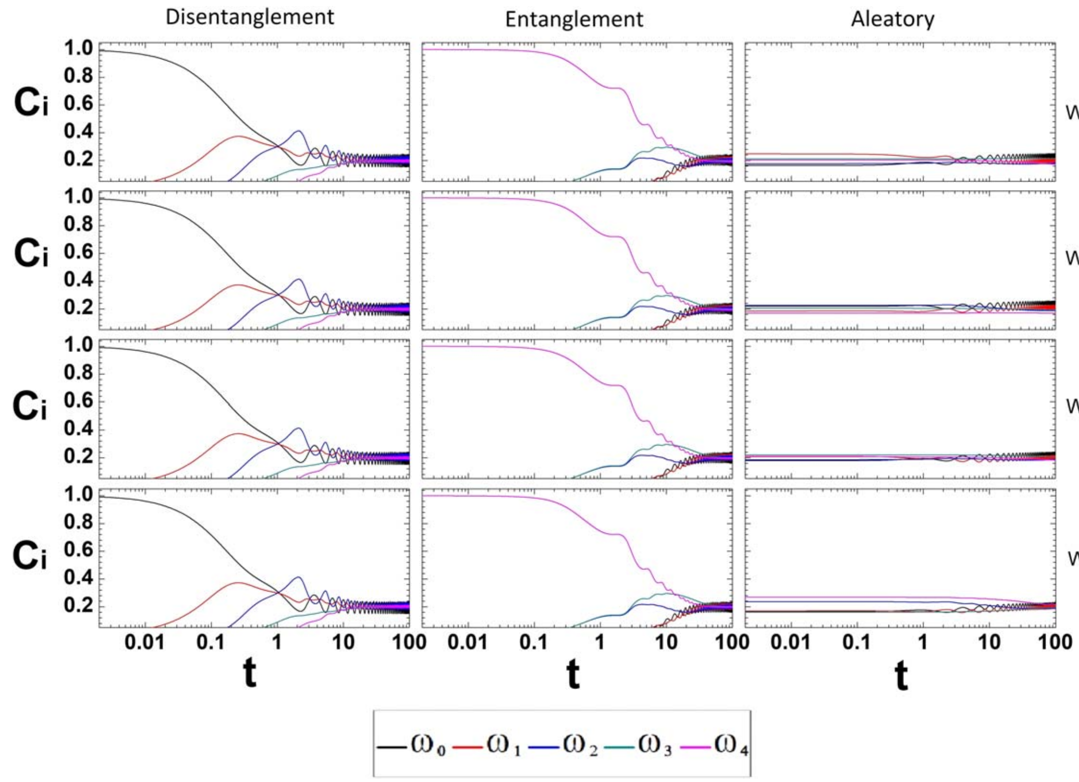

Figure 11. Influence of the Weissenberg number Wi on the time evolution of microstate concentrations for different entanglement scenarios with $De = 1, \beta = 0.1, b = 50, A = 1, B = 1, Re = 0.001$ and $N_f = 1500$.

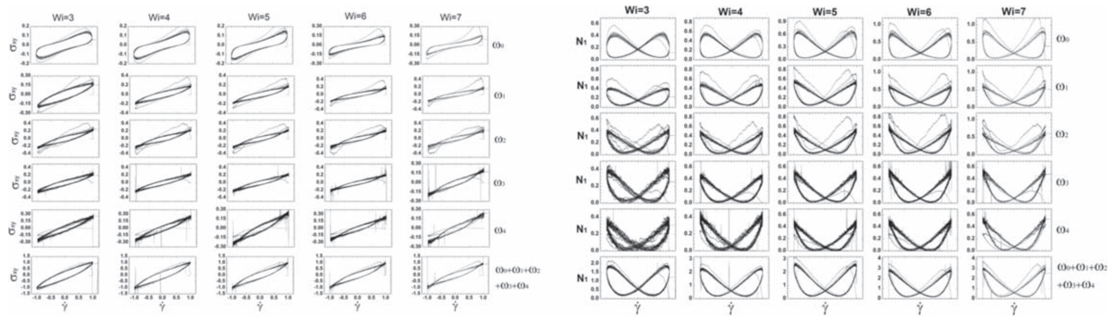

Figure 12. Influence of the Weissenberg number Wi on the Lissajous curves for the shear stress σ_{xy} (left) and N_1 (right) versus $\dot{\gamma}$ for each microstate of a disentanglement structured network with $De = 1, \beta = 0.1, b = 50, A = 1, B = 1, Re = 0.001$ and $N_f = 1500$.

requirements. Because of this, several cases in figure 15 show a sudden increase in the concentration of the simplest microstates such as ω_0, ω_1 and ω_2.

Figures 16–18 show the effect of the kinetic rate constants A and B on the LC for σ_{xy} and N_1 for each microstate with different entanglement scenarios under LAOS regime. For the disentanglement network, from a highly structured network ($A = 100, B = 1$) to a weakly structured network ($A = 1, B = 100$), the shape of the LC for σ_{xy} and N_1 are substantially modified and classical and different secondary loops are found. It is important to mention that the value of $b = 50$, indicating that the formation and shape of secondary loops depends on kinetics and the initial entanglement scenario. For the entanglement and aleatory networks, the changes are very similar to the previous case in terms of the shape of the Lissajous curves for σ_{xy} and N_1, besides additionally observing thixotropic behavior in various microstates. An important task of rheology is to relate kinetics and microstructure through models such as the present one and experiments. Jeyaseelan and Giacomin used a framework based on molecular entanglement kinetics to interpret the LAOS behavior of polyacrylamide and polystyrene solutions [43]. A kinetic rate equation for the balance of entanglements was capable of predicting previously reported LAOS data for these solutions. They concluded that the transient network concept provides a reasonable framework to interpret the LAOS behavior of two polymer solutions. Their predictions were

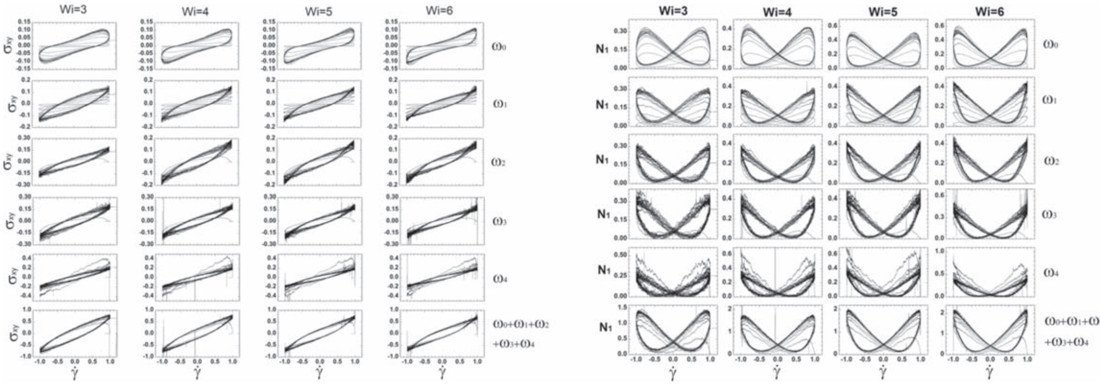

Figure 13. Influence of the Weissenberg number Wi on the Lissajous curves for the shear stress σ_{xy} (left) and N_1 (right) versus $\dot{\gamma}$ for each microstate of an entanglement structured network with $De = 1$, $\beta = 0.1$, $b = 50$, $A = 1$, $B = 1$, $Re = 0.001$ and $N_f = 1500$.

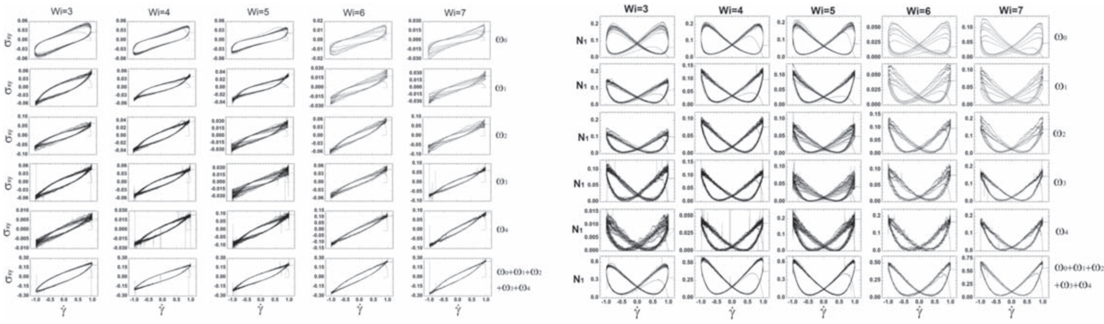

Figure 14. Influence of the Weissenberg number Wi on the Lissajous curves for the shear stress σ_{xy} (left) and N_1 (right) versus $\dot{\gamma}$ for each microstate of an aleatory structured network with $De = 1$, $\beta = 0.1$, $b = 50$, $A = 1$, $B = 1$, $Re = 0.001$ and $N_f = 1500$.

obtained for both shear and normal stresses, manifesting secondary loops at severe conditions due to non-affine deformation. Szopinski and Luinstra described the nonlinear flow behavior of aqueous carboxymethyl hydroxypropyl guargum (CMHPG) and non-ionic hydroxypropyl guar gum (HPG) solutions [44]. The high molecular weight of guar gum and its derivatives in combination with the formation of superstructures/aggregates in aqueous solutions leads to excellent water-thickening properties, and makes it useful in food, agricultural and textile applications. The influence and breakup of superstructures/aggregates gives a rheological fingerprint, a function of the applied deformation and time scale (Pipkin space).

The effect of A and B on the LC of the elastic projection of the shear stress for different entanglement scenarios is shown in figure 19. In the elastic projection of the shear stress the LC approaches a rectangle or a flag which is related with the formation of secondary loops. This flag form is also modified by the kinetics and entanglement scenario. Similar elastic projection was reported by Ewoldt *et al* who developed experiments for two complex fluids, a pseudoplastic shear-thinning xanthan gum solution and an elastoviscoplastic invert-emulsion drilling fluid [45]. They explored how the yielding response depends on both strain amplitude and frequency of deformation. Their calculations with simple pseudoplastic (viscous Carreau) and elastoplastic (elastic Bingham) models, as well as experimental measurements, correspond to increasingly rectangular LC. The LC of the raw measured stress as a function of the strain indicated an initial transient response which quickly settles into steady oscillatory orbits. Li and Wang investigated nonlinear behavior in LAOS for four different polymeric materials using simultaneous conventional rheometric measurements and particle tracking velocimetric observations. They emphasized that for the four examples considered, the nonlinearity in LAOS often arises in complex fluids due to the time dependent rearrangement of their microstructures in response to LAOS [46]. They concluded that the structural change induced by LAOS may not be generally described by classical constitutive models, where all material parameters are constant with respect to both space and time.

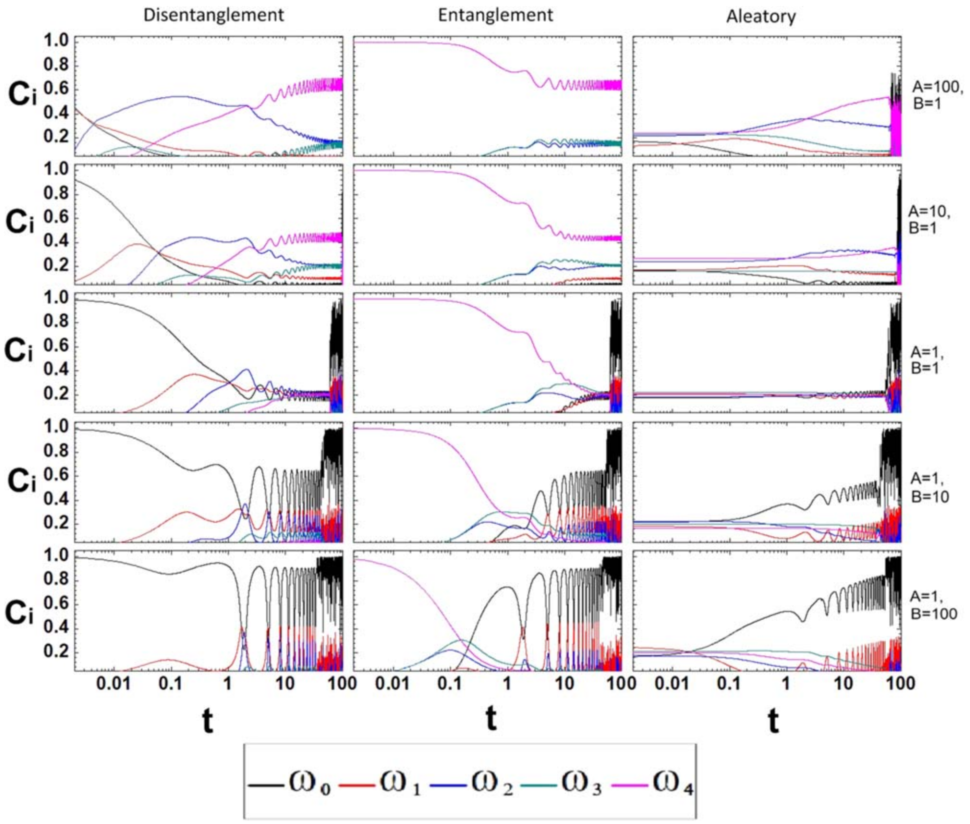

Figure 15. Influence of the kinetic rate constants A and B on the time evolution of microstate concentrations for different entanglement scenarios with $Wi = 7$, $De = 1$, $\beta = 0.1$, $b = 50$, $Re = 0.001$ and $N_f = 1500$.

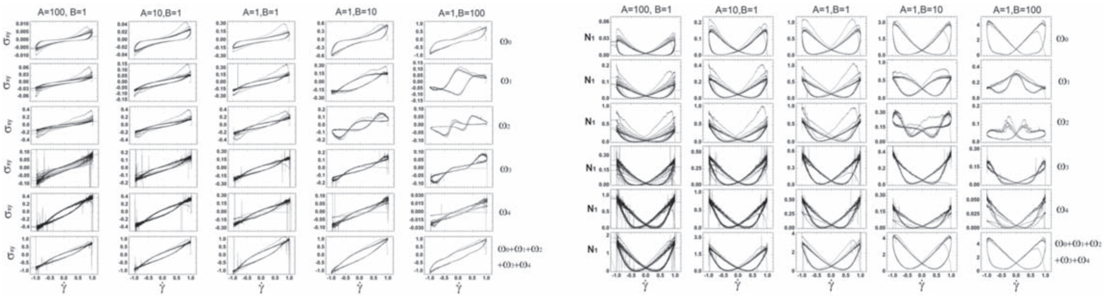

Figure 16. Influence of the kinetic rate constants A and B on the Lissajous curves for each microstate for σ_{xy} (left) and N_1 (right) versus $\dot{\gamma}$ of a disentanglement structured network with $Wi = 7$, $De = 1$, $\beta = 0.1$, $b = 50$, $Re = 0.001$ and $N_f = 1500$.

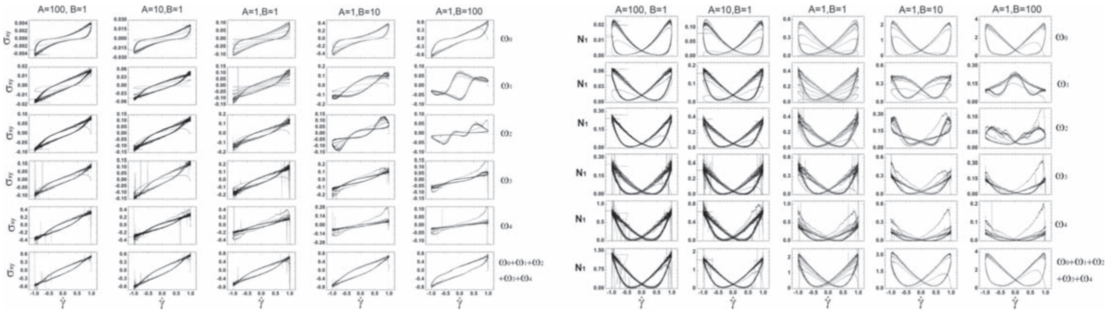

Figure 17. Influence of the kinetic rate constants A and B on the Lissajous curves for each microstate for σ_{xy} (left) and N_1 (right) versus $\dot{\gamma}$ of a entanglement structured network with $Wi = 7$, $De = 1$, $\beta = 0.1$, $b = 50$, $Re = 0.001$ and $N_f = 1500$.

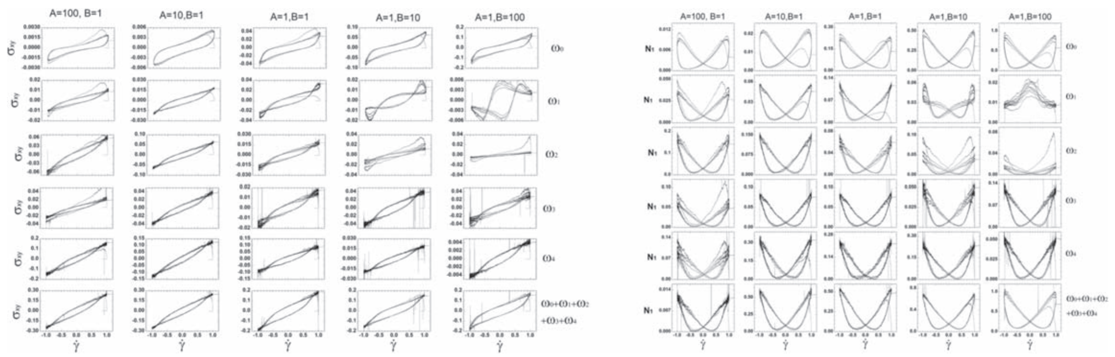

Figure 18. Influence of the kinetic rate constants A and B on the Lissajous curves for each microstate for σ_{xy} (left) and N_1 (right) versus γ_0 of a aleatory structured network with $Wi = 7$, $De = 1$, $\beta = 0.1$, $b = 50$, $A = 1$, $Re = 0.001$ and $N_f = 1500$.

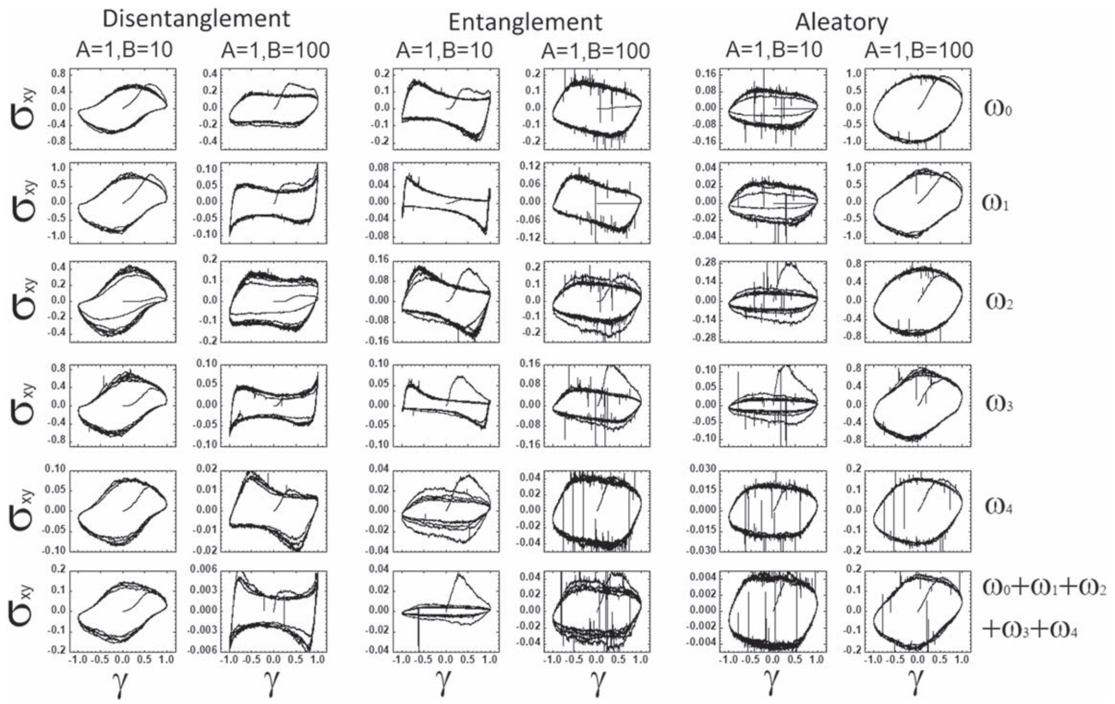

Figure 19. Influence of the kinetic rate constants A and B on the Lissajous curves for each microstate for σ_{xy} versus γ for different entanglement scenarios with $Wi = 7$, $De = 1$, $\beta = 0.1$, $b = 50$, $Re = 0.001$ and $N_f = 1500$.

8. Conclusions

In this paper numerical simulations of complex fluids under SAOS and LAOS have been presented. The basis of the numerical simulations is a micro-macro solver in which the microscopic part of the method uses the method of Brownian configuration fields in conjunction with transient network dynamics. The effect of the principal model parameters such as viscosity ratio β, chain length b, elasticity level Wi, kinetic rate constants A and B, for different initial entanglement scenarios (entangled, disentangled and aleatory) was analyzed. The Wi/De ratio accurately describes the flow conditions: LAOS $\left(\frac{Wi}{De} \geqslant 1\right)$ and SAOS $\left(\frac{Wi}{De} < 1\right)$.

Modification of β, b and Wi generates small changes in the evolution of the microstate concentrations. Substantial changes are obtained by modifying the kinetic rate constants (A and B) and the initial entanglement scenario. Increasing Wi with ($A = 1$ and $B = 1$) and the rest of the variables constant on the Lissajous curves, increases the nonlinear response and thixotropic behavior can be found for some microstates.

The FENE model using the BCFM under LAOS requires larger values of Wi/De and short extension lengths to generate self-intersection of the LC which form secondary loops. The FENE / transient network model using BCFM under LAOS considered the interaction of microstates (microstructures) immersed in a Newtonian fluid. This model is able to predict experimental results using different initial conditions and kinetic schemes. The secondary loops are strongly dependent on the kinetics and are mainly generated when the destruction is faster than the creation of microstructures ($A < B$).

The present work provides an important tool for characterizing complex fluids with different initial conditions under SAOS and LAOS regimes. It enables the behavior of material rheological fuctions to be predicted and the relationship between microstructure and macroscopic behavior to be understood.

Acknowledgments

This work was supported by the Instituto Politécnico Nacional in Mexico under grant numbers SIP-20221783 and SIP-20221572. A. G-L. gratefully acknowledges the proyects CI2270-UNAM and PE103923-UNAM for financial support.

Data availability statement

The data that support the findings of this study are available upon reasonable request from the authors.

Conflict of interest

The authors declare that they have no conflict of interest.

ORCID iDs

R O Vargas https://orcid.org/0000-0002-7042-6563
A Gómez-López https://orcid.org/0000-0001-8419-3839
J P Escandón https://orcid.org/0000-0003-2210-5324
R Mil-Martínez https://orcid.org/0000-0002-6713-464X
T N Phillips https://orcid.org/0000-0001-6455-1205

References

[1] Hyun K, Wilhelm M, Klein C O, Cho K S, Nam J G, Ahn K H, Lee S J, Ewoldt R H and McKinley G H 2011 A review of nonlinear oscillatory shear tests: Analysis and application of large amplitude oscillatory shear (LAOS) *Prog. Polym. Sci.* **36** 1697–753
[2] Hyun K, Baik E S, Ahn K H, Lee S J, Sugimoto M and Koyama K 2007 Fourier-transform rheology under medium amplitude oscillatory shear for linear and branched polymer melts *J. Rheol.* **51** 1319–42
[3] Wilhelm M 2002 Fourier-transform rheology *Macromol. Mater. Eng.* **287** 83–105
[4] Cho K S, Hyun K, Ahn K H and Lee S J 2005 A geometrical interpretation of large amplitude oscillatory shear response *J. Rheol.* **49** 747–58
[5] Klein C, Venema P, Sagis L and van der Linden E 2008 Rheological discrimination and characterization of carrageenans and starches by Fourier transform-rheology in the non-linear viscous regime *J. Non-Newton. Fluid Mech.* **151** 145–50
[6] Ewoldt R H, Hosoi A E and McKinley G H 2008 New measures for characterizing nonlinear viscoelasticity in large amplitude oscillatory shear *J. Rheol.* **52** 1427–58
[7] Rogers S A and Lettinga M P 2012 A sequence of physical processes determined and quantified in large-amplitude oscillatory shear (LAOS): Application to theoretical nonlinear models *J. Rheol.* **56** 1–25
[8] Simon A R, Erwin B M, Vlassopoulos D and Cloitre M 2011 A sequence of physical processes determined and quantified in LAOS: Application to a yield stress fluid *J. Rheol.* **55** 435–58
[9] Wyss H M, Miyazaki K, Mattsson J, Hu Z, Reichmann D R and Weitz D A 2007 Strain-rate frequency superposition: A rheological probe of structural relaxation in soft materials *Phys. Rev. Lett.* **98** 238–303
[10] Hyun K, Kim S H, Ahn K H and Lee S J 2002 Large amplitude oscillatory shear as away to classify the complex fluids *J. Non-Newton. Fluid Mech.* **107** 51–65
[11] Dealy J M and Wissbrun K F 1990 *Melt Rheology and Its Role in Plastics Processing: Theory and Applications* (Springer)
[12] Sim H G, Ahn K H and Lee S J 2003 Large amplitude oscillatory shear behavior of complex fluids investigated by a network model: a guideline for classification *J. Non-Newton. Fluid Mech.* **112** 237–50
[13] Green M S and Tobolsky A V 1946 A new approach to the theory of relaxing polymeric media. J- *Chem. Phys.* **14** 80–92
[14] Lodge A S 1956 A network theory of flow birefringence and stress in concentrated polymer solutions *Trans. Faraday Soc.* **52** 120–30
[15] Vaccaro A and Marrucci G 2000 A model for the nonlinear rheology of associating polymers *J. Non-Newton. Fluid Mech.* **92** 261–73
[16] Rincón E, Chávez A E, Herrera R and Manero O 2005 Rheological modelling of complex fluids: A transient network model with microstates *J. Non-Newton. Fluid Mech.* **131** 64–77
[17] Bird R B, Curtiss C F, Armstrong R C and Hassager O 1987 Dynamics of polymeric liquids *Kinetic Theory* (New York: Wiley) vol 2
[18] Ferrer V H, Gómez A, Ortega J A, Manero O, Rincón E, López-Serrano F and Vargas R O 2017 Modeling of complex fluids using micro-macro approach with transient network dynamics *Rheol. Acta* **56** 445–59
[19] Gómez-López A, Ferrer V H, Rincón E, Aguayo J P, Chávez A E and Vargas R O 2019 Large-amplitude oscillatory shear flow simulation for a FENE fluid *Rheol. Acta* **58** 241–60
[20] Warner H R 1972 Kinetic theory and rheology of dilute suspensions of finitely extendible dumbbells *Ind. Eng. Chem. Fund.* **11** 379–87

[21] Bird R B, Giacomin A J, Schmalzer A M and Aumnate C 2014 Dilute rigid dumbbell suspensions in large-amplitude oscillatory shear flow: Shear stress response *J. Chem. Phys.* **140** 074904

[22] Schmalzer A M, Bird R B and Giacomin A J 2015 Normal stress differences in large-amplitude oscillatory shear flow for dilute rigid dumbbell suspensions *J. Non-Newton. Fluid Mech.* **222** 56–71

[23] Lozinski A and Chauviere C 2003 A fast solver for Fokker-Planck equation applied to viscoelastic flows calculations: 2d FENE model *J. Comput. Phys.* **189** 607–25

[24] van den Brule B H A A 1993 Browian dynamics simulation of finitely extensible bead-spring chains *J. Non-Newton. Fluid Mech.* **47** 357–78

[25] Öttinger H C, van den Brule B H A A and Hulsen M A 1997 Brownian configuration fields and variance reduced CONNFFESSIT *J. Non-Newton. Fluid Mech.* **70** 255–61

[26] vom Scheidt J 1989 Introduction to stochastic differential equations *Z. angew Math. Mech.* **69** 258

[27] Laso M and Öttinger H C 1993 Calculation of viscoelastic flow using molecular models: the connffessit approach *J. Non-Newton. Fluid Mech.* **47** 1–20

[28] Melchior M and Öttinger H C 1995 Variance reduced simulations of stochastic differential equations *J. Chem. Phys.* **103** 9506–9

[29] Phillips T N and Smith K D 2006 A spectral element approach to the simulation of viscoelastic flows using Brownian configuration fields *J. Non-Newton. Fluid Mech.* **138** 98–110

[30] Vargas R O, Manero O and Phillips T N 2009 Viscoelastic flow past confined objects using a micro-macro approach *Rheol. Acta* **48** 373–95

[31] Öttinger H C 1995 *Stochastic Processes in Polymeric Fluids : Tools and Examples for Developing Simulation Algorithms.* (Springer)

[32] Wendt J F and Anderson J D 2009 *Computational Fluid Dynamics : An Introduction* (Springer)

[33] Smith K D and Sequeira A 2011 Micro-macro simulations of a shear-thinning viscoelastic kinetic model: applications to blood flow *Appl. Anal.* **90** 227–52

[34] Mas R and Magnin A 1997 Experimental validation of steady shear and dynamic viscosity relation for yield stress fluids *Rheol. Acta* **36** 49–55

[35] Tiu C, Guo J and Uhlherr P H T 2006 Yielding behaviour of viscoplastic materials *J. Ind. Eng. Chem.* **12** 653–62

[36] Saengow C, Giacomin A J and Kolitawong C 2015 Exact analytical solution for large-amplitude oscillatory shear flow *Macromol. Theory Simul.* **24** 352–92

[37] Deshpande A P, Krishnan J M and Kumar S 2010 *Rheology of Complex Fluids* (New York: Springer)

[38] Khair A S 2016 Large amplitude oscillatory shear of the Giesekus model *J. Rheol.* **60** 257–66

[39] Gurnon A K and Wagner N J 2012 Large amplitude oscillatory shear (LAOS) measurements to obtain constitutive model parameters: Giesekus model of banding and nonbanding wormlike micelles *J. Rheol.* **56** 333–51

[40] Férec J, Heuzey M C, Ausias G and Carreau P J 2008 Rheological behavior of fiber-filled polymers under large amplitude oscillatory shear flow *J. Non-Newton. Fluid Mech.* **151** 89–100

[41] Anvari M and Joyner H S M 2019 Concentrated emulsions as novel fat replacers in reduced-fat and low-fat cheddar cheeses. part 2. large amplitude oscillatory shear behavior *Int. Dairy J.* **91** 137–46

[42] Tong K, Xiao G, Cheng W, Chen J and Sun P 2018 Large amplitude oscillatory shear behavior and gelation procedure of high and low acyl gellan gum in aqueous solution *Carbohydr. Polym.* **199** 397–405

[43] Jeyaseelan R S and Giacomin A J 2008 Network theory for polymer solutions in large amplitude oscillatory shear *J. Non-Newton. Fluid Mech.* **148** 24–32

[44] Szopinski D and Luinstra G A 2016 Viscoelastic properties of aqueous guar gum derivative solutions under large amplitude oscillatory shear (LAOS) *Carbohydr. Polym.* **153** 312–9

[45] Ewoldt R H, Winter P, Maxey J and McKinley G H 2010 Large amplitude oscillatory shear of pseudoplastic and elastoviscoplastic materials *Rheol. Acta.* **49** 191–212

[46] Li X and Wang S Q 2009 Nonlinearity in large amplitude oscillatory shear (LAOS) of different viscoelastic materials *J. Rheol.* **53** 1255